JACS
JOURNAL OF THE AMERICAN CHEMICAL SOCIETY
Article
pubs.acs.org/JACS

# Understanding the High Photocatalytic Activity of (B, Ag)-Codoped $TiO_2$ under Solar-Light Irradiation with XPS, Solid-State NMR, and DFT Calculations

Ningdong Feng,[†] Qiang Wang,[†] Anmin Zheng,[†] Zhengfeng Zhang,[†] Jie Fan,[‡] Shang-Bin Liu,[§] Jean-Paul Amoureux,[⊥] and Feng Deng*[,†]

[†]State Key Laboratory of Magnetic Resonance and Atomic Molecular Physics, Wuhan Center for Magnetic Resonance, Key Laboratory of Magnetic Resonance in Biological Systems, Wuhan Institute of Physics and Mathematics, Chinese Academy of Sciences, Wuhan 430071, China

[‡]Key Laboratory of Applied Chemistry of Zhejiang Province and Department of Chemistry, Zhejiang University, Hangzhou 310027, China

[§]Institute of Atomic and Molecular Sciences, Academia Sinica, P.O. Box 23-166, Taipei 10617, Taiwan

[⊥]UCCS (CNRS-8181), Batiment C7, ENSCL Lille-1 University, Villeneuve d'Ascq 59652, France

Supporting Information

**ABSTRACT:** The origin of the exceptionally high activity of (B, Ag)-codoped $TiO_2$ catalysts under solar-light irradiation has been investigated by XPS and $^{11}B$ solid-state NMR spectroscopy in conjunction with density functional theory (DFT) calculations. XPS experimental results demonstrated that a portion of the dopant Ag ($Ag^{3+}$) ions were implanted into the crystalline lattice of (B, Ag)-codoped $TiO_2$ and were in close proximity to the interstitial B ($B_{int.}$) sites, forming [$B_{int.}$−O−Ag] structural units. In situ XPS experiments were employed to follow the evolution of the chemical states of the B and Ag dopants during UV−vis irradiation. It was found that the [$B_{int.}$−O−Ag] units could trap the photoinduced electron to form a unique intermediate structure in the (B, Ag)-codoped $TiO_2$ during the irradiation, which is responsible for the photoinduced shifts of the B 1s and Ag 3d peaks observed in the in situ XPS spectra. Solid-state NMR experiments including $^{11}B$ triple-quantum and double-quantum magic angle spinning (MAS) NMR revealed that up to six different boron species were present in the catalysts and only the tricoordinated interstitial boron (T*) species was in close proximity to the substitutional Ag species, leading to formation of [T*−O−Ag] structural units. Furthermore, as demonstrated by DFT calculations, the [T*−O−Ag] structural units were responsible for trapping the photoinduced electrons, which prolongs the life of the photoinduced charge carriers and eventually leads to a remarkable enhancement in the photocatalytic activity. All these unprecedented findings are expected to be crucial for understanding the roles of B and Ag dopants and their synergistic effect in numerous titania-mediated photocatalytic reactions.

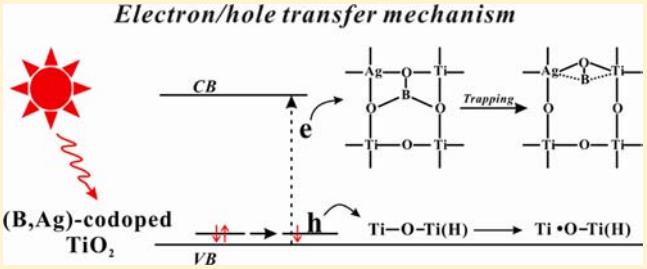


## 1. INTRODUCTION

Since the pioneered discovery of photocatalytic decomposition of water on anatase titanium dioxide ($TiO_2$),[1] the study of the semiconductor photocatalysts has drawn intensive interest in the research and development communities. However, because of the wide band gap (3.2 eV) possessed by the anatase $TiO_2$, its photocatalytic application is limited by a narrow range of irradiation light source, which falls in the ultraviolet (UV) region. It is highly desirable to develop photocatalysts that remain highly active over a wider range of radiation wavelength covering most of the solar light, which consists of UV light (300−380 nm; ca. 4%), visible light (vis, 380−780 nm; ca. 46%), and infrared light (IR, 780−3000 nm; ca. 50%). A prominent approach is to dope $TiO_2$ with transition metals (such as Fe, V, Ag, etc.)[2−4] or nonmetallic elements (such as B, N, F, etc.).[5−7] However, the former cation doping scheme tends to suffer from thermal instability and inevitable increase in photoinduced carrier recombination centers, which impairs the lifetime of the carriers. On the other hand, the latter anion doping seems to be more appropriate for the extension of photocatalytic activity of $TiO_2$ into the visible-light region than the former scheme because its impurity state is near the valence band edge, while the anion doping also introduces localized oxygen vacancies located at 0.8−0.9 eV (i.e., below the conduction band minimum),[5,8,9] leading to a low electron mobility in bulk anatase $TiO_2$ because of the localization. Thus, while both cation and anion implantations are capable of

Received: December 14, 2012
Published: January 15, 2013



dx.doi.org/10.1021/ja312205c | J. Am. Chem. Soc. 2013, 135, 1607−1616

implementing the absorption of visible light to some extent, they do not warrant enhanced activity of the doped $TiO_2$ photocatalysts in a certain region of solar light. For instance, the sole nitrogen doping of $TiO_2$ usually leads to limited visible-light activity and greatly impairs the photocatalytic activity under UV irradiation.[6] The key to develop efficient solar-light photocatalysts lies in the design and construction of effective photocatalyst structures that facilitate the separation and transfer of the photoinduced carriers.

To achieve optimal photocatalytic activities under irradiation from solar light, considerable research attention has focused on the codoping of $TiO_2$ with boron (B) and other elements. For example, it has been demonstrated[10−13] that a secondary B doping of the *x*-doped $TiO_2$ (*x* = F, N, Fe, or Ni) further invokes considerable improvement in the photocatalytic activity of the (B, *x*)-codoped catalyst. Nevertheless, the photocatalytic active structures and mechanisms of these codoped catalysts remain poorly understood, which limits the research and development of highly efficient photocatalysts. Herein, we report a novel (B, Ag)-codoped $TiO_2$ photocatalyst with extraordinary reactivity under solar-light irradiation. To gain further insight into plausible mechanisms associated with the photocatalyst, the results from density functional theory (DFT) calculations were correlated to those obtained from experimental studies, such as UV−vis absorption spectroscopy, X-ray photoelectron spectroscopy (XPS), and nuclear magnetic resonance (NMR) spectroscopy. In particular, in situ XPS was employed to follow the evolution of the chemical state of the dopants during UV−vis irradiation, while $^{11}B$ solid-state magic-angle-spinning (MAS) NMR was used to identify the local structures of the contingent dopants in various B- and Ag-doped and (B, Ag)-codoped $TiO_2$ catalysts. As a result, the exceptionally high photocatalytic activity observed for the (B, Ag)-codoped $TiO_2$ is ascribed to the synergistic effect of the B and Ag dopants.

## 2. EXPERIMENTAL AND COMPUTATIONAL METHODS

**2.1. Sample Preparation.** Various (B, Ag)-codoped $TiO_2$ samples were prepared by the solvent-thermal method. Typically, known amounts of boric acid (with molar ratios of B/Ti = 0.005, 0.02, 0.05, 0.10, and 0.20) and silver nitrate (with Ag/Ti = 0.005, 0.01, 0.03, and 0.05) were dissolved in 200 mL of an ethanol/water mixture. Subsequently, 0.033 mol of titanium(IV) isopropoxide ($Ti(O^iPr)_4$; Alfa Aesar, 95%) was added dropwise to the solution mixture under continuous stirring. The resultant translucent sol was aged for 12 h at room temperature and then transferred into a Teflon bottle for further hydrothermal treatment at 358 K for 3 h. Subsequently, the gel was cooled to room temperature, followed by filtration, drying at 473 K, and calcination treatment in air at 673 K for 4 h to obtain the final (B, Ag)-doped $TiO_2$ samples. A similar method was adopted for the preparation of the undoped (pure), B-doped, and Ag-doped $TiO_2$ catalyst samples except for the different varieties of precursors added. X-ray diffraction (Figure S1, Supporting Information) showed that the anatase $TiO_2$ phase (accompanying with a small amount of bookite phase) was predominant in the pure $TiO_2$ sample, while only the anatase phase was present in the doped $TiO_2$ samples (Figure S1), and no diffraction lines corresponding to Ag and/or $B_2O_3$ were observed, indicative of a high dispersion of dopants in the $TiO_2$ samples.

**2.2. Characterization Methods.** All UV−vis diffuse reflectance spectroscopic (DRS) experiments were carried out on a Shimadzu UV 3150 spectrophotometer using $BaSO_4$ as the reference. X-ray photoelectron spectroscopy (XPS) were conducted on a Kratos Axis Ultra delay line detector (DLD) spectrometer equipped with a monochromated Al K$\alpha$ X-ray source ( $\hbar\nu$ = 1486.6 eV), hybrid (magnetic/electrostatic) optics with a multichannel plate, and DLD. All XPS spectra were recorded using an aperture slot of 300 × 700 $\mu$m.

Solid-state $^{11}B$ one-dimensional (1D) and two-dimensional triple-quantum (2D 3Q)[14,15] magic-angle-spinning (MAS) NMR experiments were performed on a Bruker AVANCE II 400 spectrometer using a 4 mm double-resonance probe-head with a Larmor frequency of 400.13 and 128.38 MHz and a typical $\pi/2$ pulse length of 2.4 and 2.5 $\mu$s for $^1H$ and $^{11}B$, respectively. The excitation pulse length was adjusted to $\pi/12$ for the single-pulse $^{11}B$ MAS experiments with $^1H$ decoupling (field strength ca. 100 kHz), by which a total of 20 000 free-induction-decay (FID) signals were accumulated with a repetition time of 2 s. The $^{11}B$ triple-quantum z-filtering with fast amplitude modulation (3QZ-FAM) MAS NMR spectra were recorded with the pulse sequence proposed by Vega and co-workers,[16,17] in which 64 $t_1$ increments of 10 $\mu$s in the $F_1$ dimension were acquired (collecting 1344 scans per $t_1$ increment) with a recycle delay of 2 s under a sample spinning rate of 15 kHz. All $^{11}B$ NMR chemical shifts were referenced to that of $H_3BO_3$ (0.1 M).

$^{11}B$ double-quantum (DQ) MAS NMR[18,19] experiments were carried out on a Bruker AVANCE III 800 spectrometer with a 3.2 mm triple-resonance (HXY) MAS probe at a sample spinning rate of 21.5 kHz. The Larmor frequency is 256.76 MHz for $^{11}B$. A CT-selective $\pi/2$ pulse of 17 $\mu$s was used for the DQ MAS experiments, and the signal sensitivity was enhanced by initiating each transient by the FAM scheme. DQ coherences were excited and reconverted by using the $BR2_2^1$ pulse sequence[20] with $\tau_{exc} = \tau_{rec}$ = 186.04 $\mu$s, following the general scheme of 2D multiple-quantum (MQ) spectroscopy of dipolar-coupled quadrupolar spins. The rotor-synchronized increment interval in the indirect dimension was set to 46.51 $\mu$s, and the two-dimensional data sets consisted of $30t_1 \times 400t_2$ points. A total of 13054 and 14080 FIDs for each $t_1$ increment with a recycle delay of 1.0 s was acquired for the 10% B-doped and (10% B, 3% Ag)-codoped $TiO_2$ samples, respectively.

**2.3. Computational Models and Methods.** A 2 × 2 × 2 supercell of anatase $TiO_2$ was used to model the structures of pure and doped-$TiO_2$, namely those incorporated with substitutional Ag, tricoordinate interstitial boron (T*), and Ag−O−T*. During the structure optimizations, the electron correlation effects were modeled using the generalized gradient approximation (GGA) level with PBEsol combination of exchange and correlation functionals.[21] PBEsol is intended to improve PBE for equilibrium properties such as bond lengths and lattice parameters.[22] The ultrasoft pseudopotentials were used for the structure optimizations. In addition, a plane-wave cutoff energy of 340 eV and a 2 × 2 × 1 Monkhorst-Pack *k*-point grid[23] were adopted to sample the Brillouin zone. During structure optimization, the unit cell parameters (cell shape and volume) and all the O−Ti atoms around the dopant B and Ag atoms were allowed to relax to their stable positions. Based on the optimized structures, the spin-polarized density of state (DOS) were calculated by the GGA/PBE level using a 2 × 2 × 1 Monkhorst-Pack *k*-point, and the plane-wave cutoff energies were set to 340 eV for the DOS. All structure optimizations and DOS calculations were performed by CASTEP 5.0 codes utilizing the parallel 16 CPU in IBM-1350 cluster facilitated by the National Center for High-performance Computing (NCHC) in Taiwan.

## 3. RESULTS AND DISCUSSION

**3.1. Optical Absorption and Photocatalytic Activity.** Figure 1 displays the UV−vis absorption spectra of undoped and doped $TiO_2$ samples. The intensity of visible-light absorption between 380 and 780 nm gradually increases with the amount of doped B increasing from 0 to 10% in the solely B-doped $TiO_2$ photocatalysts (Figure 1, bottom). It was previously reported that two types of lattice B species, substitutional boron and pseudotetrahedral coordinated interstitial boron (Q*) in the B-doped $TiO_2$, tend to result in visible-light absorption.[7,13] Our previous studies demonstrated that the presence of Q* species would be responsible for a decrease in band gap and hence favor the absorption in the visible-light region.[7] Compared to the solely B-doped $TiO_2$ and


dx.doi.org/10.1021/ja312205c | J. Am. Chem. Soc. 2013, 135, 1607−1616

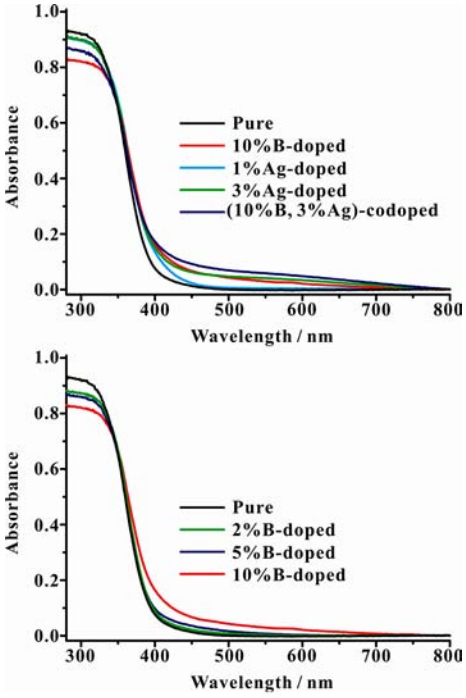


**Figure 1.** UV−vis absorption spectra of various $TiO_2$ samples. Upper: pure, 1% Ag-doped, 3% Ag-doped, 10% B-doped, and (10% B, 3% Ag)-codoped $TiO_2$ samples. Bottom: B-doped $TiO_2$ samples with different boron content.

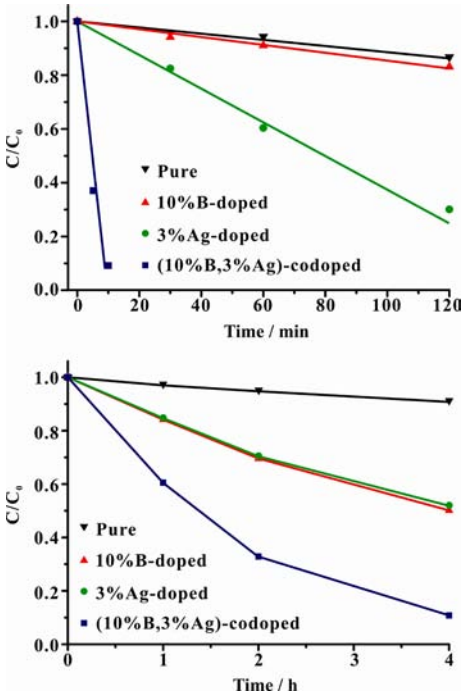


**Figure 2.** Photodegradation curves of methylene blue on pure, 10% B-doped, 3% Ag-doped, and (10% B, 3% Ag)-codoped $TiO_2$ upon irradiation with solar light (upper) and visible light (bottom; $\lambda > 420$ nm). The concentrations of methylene blue were determined by the observed optical intensities at $\lambda = 665$ nm.

pure $TiO_2$, the visible-light absorption can be further enhanced upon additional Ag doping (Figure 1, upper).

The photocatalytic activities of various catalysts were further evaluated by monitoring the photodegradation of a typical dye, namely methylene blue (MB), under irradiation from different light sources. Consequently, the catalytic activities of pure, solely B- and Ag-doped, and (B, Ag)-codoped $TiO_2$ catalysts under irradiation from solar light (Figure 2, upper) and visible light (Figure 2, bottom) were compared. It is indicative that notable increases in the activities of (B, Ag)-codoped $TiO_2$ compared to the pure and solely B- and Ag-doped catalysts can be inferred regardless of the applied light sources. For example, the activities of assorted photocatalysts depicted in Figure 2 clearly show that the MB photodegradation observed for the (10% B, 3% Ag)-codoped $TiO_2$ is nearly completed within ca. 10 min under solar-light irradiation or ca. 4 h under visible-light irradiation. On the other hand, a much slower photodegradation was observed for solely 10% B-doped or 3% Ag-doped and for pure $TiO_2$ catalysts. It is noteworthy that compared with pure, solely B-doped, or Ag-doped $TiO_2$ photocatalysts, the (B, Ag)-codoped $TiO_2$ also exhibits exceptionally high photoactivity in energetically uphill reactions, such as water splitting in the presence of methanol solution (Figure S2, Supporting Information).

The kinetic analyses of MB photodegradation and the surface area data of the samples are listed in Table 1. Compared to the 3% Ag-doped $TiO_2$, the photocatalytic activity of (10% B, 3% Ag)-codoped $TiO_2$ can be enhanced by ca. 20 times under solar-light irradiation or ca. 3.9 times under visible-light irradiation (Table 1). However, the surface areas and the adsorption curve of methylene blue on the two $TiO_2$ samples in dark are similar (see Table 1, and Figure S3, Supporting Information). This might indicate that it is the charge carrier

**Table 1. Specific Surface Area and Normalized Kinetic Constants of Photocatalysts under Solar-Light and Visible-Light Irradiation**

| samples | BET surface area ($m^2/g$) | normalized kinetic constant[a] ($\times 10^{-5}$ $min^{-1}$) solar-light | visible-light |
|---|---|---|---|
| pure $TiO_2$ | 159 | 0.8 | 0.3 |
| 10% B-doped $TiO_2$ | 149 | 1.1 | 1.9 |
| 3% Ag-doped $TiO_2$ | 106 | 9.5 | 2.8 |
| (10% B, 3% Ag)-codoped $TiO_2$ | 112 | 205.6 | 10.8 |

[a]Normalized with respect to the specific surface area.

transfer in bulk and surface rather than the adsorption of methylene blue or the following reaction of the adsorbed species that leads to the exceptionally high activity of (B, Ag)-codoped $TiO_2$.

**3.2. Chemical States and Electronic Structure Studied by XPS.** Figure 3 (left) shows the Ag 3d XPS spectra of 3% Ag-doped, (2% B, 3% Ag)-codoped, and (10% B, 3% Ag)-codoped $TiO_2$ samples. It can be seen that the Ag 3d XPS spectrum (Figure 3a) of 3% Ag-doped consist of two major peaks at 374.2 and 368.2 eV, corresponding to Ag $3d_{3/2}$ and Ag $3d_{5/2}$ binding energies, respectively, being indicative of the sole presence of metallic Ag ($Ag^0$) in the sample.[24,25] Upon introduction of the second dopant (B) into the Ag-doped $TiO_2$, a new Ag $3d_{5/2}$ XPS shoulder peak appears at 366.5 eV in Figure 3b, probably corresponding to a new Ag species in the (B, Ag)-codoped $TiO_2$ photocatalyst. Thus far, considerable studies have been carried out on the structures of Ag species with XPS, aiming to reveal their correlations with the observed


dx.doi.org/10.1021/ja312205c | J. Am. Chem. Soc. 2013, 135, 1607−1616

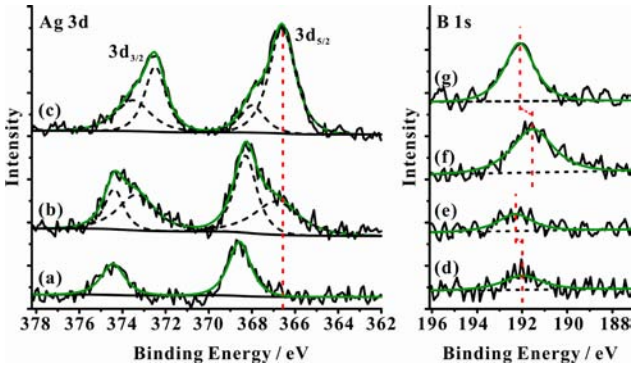


**Figure 3.** XPS spectra of various $TiO_2$ samples. Left: Ag 3d spectra of (a) 3% Ag-doped, (b) (2% B, 3% Ag)-codoped, and (c) (10% B, 3% Ag)-codoped $TiO_2$ samples. Right: B1s spectra of (d) 2% B-doped, (e) (2% B, 3% Ag)-codoped, (f) 10% B-doped, and (g) (10% B, 3% Ag)-codoped $TiO_2$ samples.

photocatalytic properties. Accordingly, it was found[26−28] that the chemical states of Ag in Ag-doped $TiO_2$ samples exist mainly as $Ag^0$ (metallic Ag) and $Ag^+$ ($Ag_2O$), associated with the Ag $3d_{5/2}$ XPS signals at ca. 368.2 and 367.6 eV, respectively. Recently, some research studies[25,29,30] also validated the existence of $Ag^{2+}$ (AgO) in Ag-doped $TiO_2$, which was associated with a Ag $3d_{5/2}$ XPS signal at 367.0 eV. As such, the Ag $3d_{5/2}$ XPS signal at 366.5 eV in Figure 3b can be attributed to a chemical state of $Ag^{3+}$, which was first found in the doped $TiO_2$ photocatalysts. Previous works[31] also reported the existence of $Ag^{3+}$ in form of $Ag_2O_3$ which could easily decompose into $Ag_2O$ and metallic Ag at room temperature in the air. In our (B, Ag)-codoped $TiO_2$ samples, the $Ag^{3+}$ species may exist as surface Ag oxide ($Ag_2O_3$) or substitutional Ag formed by substitution of Ti sites by Ag atoms in the crystalline lattice (also see the following). Because no diffraction lines corresponding to $Ag_2O_3$ were observed in our XRD experiments, we ascribed the $Ag^{3+}$ species to the substitutional Ag species. It is noteworthy that the intensity of the Ag $3d_{5/2}$ XPS signal at 366.5 eV gradually increases with the amount of doped B increasing from 2% to 10% in the (B, Ag)-codoped $TiO_2$ photocatalysts (Figure 3b and 3c), which suggests that the additional B doping favors the formation of the substitutional Ag species. Likewise, a similar variation trend was observed for the Ag $3d_{3/2}$ XPS signal after the introduction of B dopant into the Ag-doped $TiO_2$. According to our photocatalysis experiments (Figure S4, Supporting Information), the photocatalytic activity of ($x$% B, 3% Ag)-codoped $TiO_2$ samples ($x$ = 2, 5, 10) increases significantly with the content of dopant B. Thus, it can be concluded that the new Ag species may be the active sites for the highly photocatalytic activity. However, their detailed structures need further investigations.

Figure 3 (right) shows the B 1s XPS spectra of solely B-doped and (B, Ag)-codoped $TiO_2$ photocatalysts, in which a signal in the range of 191.5−192.3 eV is observable. Three kinds of B dopants with binding energy of ca. 190.6, 191.6, and 193.0 eV were previously reported for solely B-doped $TiO_2$.[7,10−13,32,33] The signal at 190.6 eV was ascribed to B−Ti−O structure (called as substitutional B), and the signal at 193.0 eV to $B_2O_3$ structure at the $TiO_2$ surface. However, the assignment of the signal at ca. 191.6 eV remains controversial. For instance, some researchers ascribed the peak to the substitutional B in the anatase $TiO_2$,[10,13,33] whereas others attributed it to B weaving into the interstitial sites of the $TiO_2$ lattice (Ti−O−B, called as interstitial B).[7,32] Herein, according to our following NMR results, we attribute the B 1s XPS peaks, observed in the range of 191.5−192.3 eV for the solely B-doped and (B, Ag)-codoped $TiO_2$ photocatalysts, to the existence of interstitial B ($B_{int.}$). It is noteworthy that a blueshift of the B 1s XPS peak from 192.0 to 192.3 eV is observable upon introducing 3% Ag into the 2% B-doped $TiO_2$ (Figure 3d and 3e). Similarly, a larger blueshift of the B 1s XPS peak from 191.5 to 192.1 eV is also evident after doping 3% Ag into the 10% B-doped $TiO_2$ (Figure 3f and 3g), which can be ascribed to the close proximity of the substitutional Ag species to the interstitial B (i.e., the formation of [$B_{int.}$−O−Ag]). In addition, the B 1s XPS peak of solely B-doped $TiO_2$ shifts from 192.0 to 191.5 eV upon increasing the amount of B dopant from 2% to 10% (Figure 3d and 3f), which should be associated with the contingent increase in interstitial B species.

The presence of interstitial B in the crystal lattice of anatase $TiO_2$ is prone to form defects around it due to the imbalance of local charges,[34] and the defects (such as distortion of the lattice, and oxygen and titanium vacancies) can provide enough space for implanting Ag into the (B, Ag)-codoped $TiO_2$ lattice by substituting the Ti site, forming the substitutional Ag. The more interstitial B, the more defects, and thus the more substitutional Ag species. This suggests that the presence of interstitial B is a prerequisite for the formation of substitutional Ag species around it, which means that the amount of substitutional Ag species should be equal to that of [$B_{int.}$−O−Ag] structural units. The amount of substitutional Ag species can be determined by XPS. For the (10% B, 3% Ag)-codoped $TiO_2$ sample, the amount of [$B_{int.}$−O−Ag] structure units is about 2.55%; that is, 85% of the total dopant Ag exists as substitutional Ag while 15% of the total dopant Ag as metallic Ag. The curve of photocatalytic kinetic constants as a function of content of [$B_{int.}$−O−Ag] structural units is shown in the Figure 4 for the various ($x$% B, 3% Ag)-codoped $TiO_2$ photocatalysts with $x$ = 0, 2, 5, 10. Most interestingly, the photocatalytic activity increases with increasing the content of [$B_{int.}$−O−Ag] units. This unambiguously demonstrates that these sites are crucial for the remarkable improvement of photoactivity.

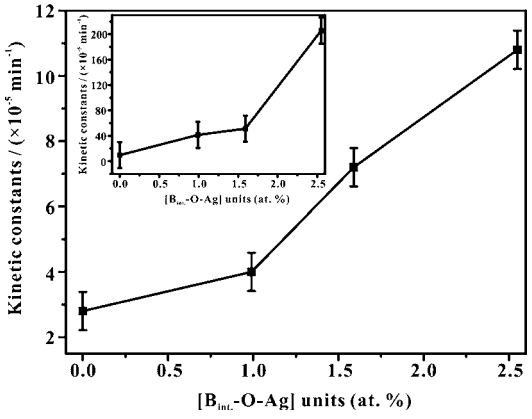


**Figure 4.** Photocatalytic kinetic constants upon visible-light irradiation normalized for specific surface area as a function of [$B_{int.}$−O−Ag] structural unit. Inset: the corresponding data upon solar-light irradiation.

**3.3. Evolution of Chemical State upon Irradiation Monitored by in Situ XPS.** To clarify the correlations

between the photocatalytic activity and structure of the dopants, in situ XPS experiments were performed on the various $TiO_2$ samples to follow the evolution of chemical state of the dopants under UV–vis irradiation (see Figure 5). Prior

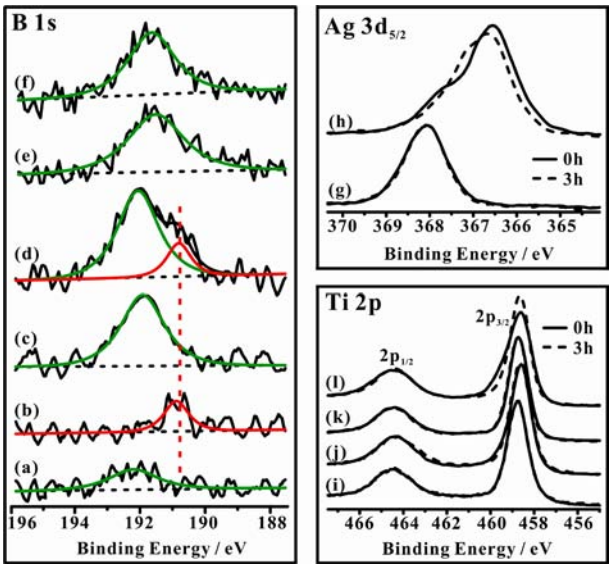


**Figure 5.** In situ XPS spectra of various $TiO_2$ samples. Left: In situ B 1s XPS spectra of (a, b) (2% B, 3% Ag)-codoped, (c, d) (10% B, 3% Ag)-codoped, and (e, f) 10% B-doped $TiO_2$ samples before (a, c, e) and after (b, d, f) UV–vis irradiation for 3 h. Right, upper: In situ Ag $3d_{5/2}$ XPS spectra of (g) 3% Ag-doped and (h) (10% B, 3% Ag)-codoped $TiO_2$ samples before (solid lines) and after (dotted lines) UV–vis irradiation for 3 h. Right, bottom: In situ Ti 2p XPS spectra of (i) pure, (j) 10% B-doped, (k) 3% Ag-doped, and (l) (10% B, 3% Ag)-codoped $TiO_2$ samples before (solid lines) and after (dotted lines) UV–vis irradiation for 3 h.

to the irradiation, the binding energy (BE) observed for the B 1s peak of the (2% B, 3% Ag)-codoped $TiO_2$ is at 192.2 eV (Figure 5a). Interestingly, a notable redshift of the peak to 191.0 eV was observed when the sample was irradiated by UV–vis for 3 h (Figure 5b), and this process is reversible. A similar photoinduced shift of the B 1s peak was also observable for the (10% B, 3% Ag)-codoped $TiO_2$ catalyst; that is, a part of the BE of B 1s peak shifts from 192.0 to 190.8 eV after the irradiation (Figure 5c and 5d). Such a photoinduced shift may be attributed to shallow trapping of photoinduced electrons by specific B sites during the UV–vis irradiation. Likewise, similar phenomena can also be inferred for the XPS spectra observed for the Ag $3d_{5/2}$ (photoinduced shift from 366.5 to 367.4 eV, Figure 5h) and Ti $2p_{3/2}$ (photoinduced shift from 460.0 to 458.9 eV, Figure 5l) chemical states of the (10%B, 3%Ag)-codoped $TiO_2$ before and after the UV–vis irradiation. Again, such photoinduced shifts observed after UV–vis irradiation may be ascribed to trapping of photoinduced electrons by the substitutional Ag species ($Ag^{3+}$) and the specific Ti sites (that are around the substitutional Ag sites). Nevertheless, the photoinduced shift was observed neither in the Ti 2p chemical states of the pure (Figure 5i), B-doped (Figure 5j), and Ag-doped (Figure 5k) $TiO_2$ nor in the B 1s chemical states of the solely B-doped $TiO_2$ (Figure 5e and 5f) and the Ag 3d chemical states of Ag-doped $TiO_2$ (Figure 5g) samples. This is probably due to the rapid recombination of photoinduced holes and electrons in the pure and the solely B- or Ag-doped photocatalysts.[7]

Therefore, boron and silver codoping should be responsible for the observed photoinduced shifts that are due to trapping of photoinduced electron by the specific B and the substitutional Ag sites, whereas isolated B sites in solely B-doped $TiO_2$ and $Ag^0$ sites in solely Ag-doped $TiO_2$ do not lead to such photoinduced shifts. It can be anticipated that the observed photoinduced shifts are due to the presence of $[B_{int.}–O–Ag]$ structural units in the lattice of (B, Ag)-codoped $TiO_2$, which may provoke mixing of chemical states to form new states due to contribution of the Ag 4d and B 2p states in the band gap (see the following DFT calculations). Consequently, the photoinduced electrons are more accessible to the new structural units, which can act as shallow traps during the UV–vis irradiation. Generally, trapping and recombination of charge carriers are competitive processes. However, trapping of charge carriers by $[B_{int.}–O–Ag]$ units is predominant in the process of bulk and surface charge carrier transfer, which may prolong the life of the photoinduced charge carriers and eventually lead to enhancement in catalytic activity of the (B, Ag)-codoped $TiO_2$ photocatalysts. Otherwise, poor photoactivity would be achieved.

**3.4. Characterization of Dopants Environment by Solid-State NMR.** Conventional 1D and 2D 3Q[14,15] solid-state $^{11}B$ MAS NMR experiments were performed at 9.4 T magnetic field to gain information on the local structures of dopants in various doped $TiO_2$ catalysts. Figure 6 displays the $^{11}B$ 3QZ-FAM MAS NMR[16,17] spectra of the 10% B-doped and (10% B, 3% Ag)-codoped $TiO_2$ samples. For the solely B-doped $TiO_2$, at least five different B environments (or sites; denoted as $B_k$, where $k$ = 1–5) may be resolved (Figure 6a),

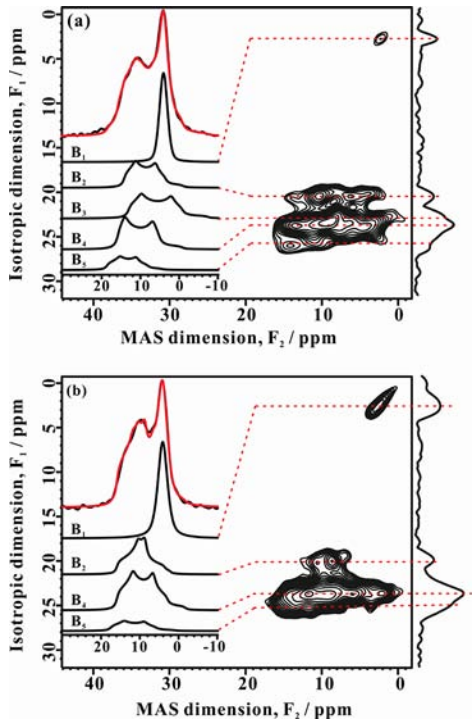


**Figure 6.** 3QZ-FAM MAS NMR spectra (sheared) of (a) 10% B-doped and (b) (10% B, 3% Ag)-codoped $TiO_2$ samples recorded at 9.4 T with a sample rotation rate of 15.0 kHz. The experimental (in black) and simulated (in red) 1D $^{11}B$ MAS spectra are depicted as insert (left-top) together with the deconvoluted spectra corresponding to various B environments.


dx.doi.org/10.1021/ja312205c | J. Am. Chem. Soc. 2013, 135, 1607–1616

**Table 2. NMR Parameters for Various Boron Species in 10% B-Doped and (10% B, 3% Ag)-Codoped $TiO_2$ Catalysts (see Supporting Information for more details)**

| | 10% B-doped | | | | (10% B, 3% Ag)-codoped | | | |
|---|---|---|---|---|---|---|---|---|
| site | $\delta_{iso}$ (ppm) | QCC (MHz) | $\eta$ | $\delta_{MAS}$ (ppm) | $\delta_{iso}$ (ppm) | QCC (MHz) | $\eta$ | $\delta_{MAS}$ (ppm) |
| $B_1$ | 2.8 | – | – | 2.3[a] | 2.9 | – | – | 2.4[a] |
| $B_2$ | 16.8 | 2.24 | 0.32 | 14.3[b] | 16.9 | 2.00 | 0.75 | 14.1[b] |
| $B_3$ | 15.9 | 2.68 | 0.26 | 13.5[b] | – | – | – | – |
| $B_4$ | 18.6 | 2.41 | 0.17 | 15.6[b] | 18.2 | 2.38 | 0.40 | 15.3[b] |
| $B_5$ | 20.0 | 2.20 | 0.40 | 16.5[b] | 19.7 | 2.31 | 0.35 | 16.5[b] |

[a]The apparent chemical shifts (the center of gravity of the signals in 1D NMR spectrum, denoted as $\delta_{MAS}$ in Table 2) directly obtained from the 1D NMR spectra of 18.8 T. [b]The apparent chemical shifts derived by fitting the 1D NMR spectra of 18.8 T with aid of the NMR parameters obtained from the NMR spectra of 9.4 T.

which may be utilized for the deconvolution of the 1D $^{11}B$ MAS spectrum (Figure 6a, insert) to attain the contingent NMR parameters, viz. $\delta_{iso}$, QCC, and $\eta$ associated with various B sites, as summarized in Table 2. In our previous study on B-doped and (B, N)-codoped $TiO_2$,[7] the signals corresponding to $B_1$ and $B_4$ at $\delta_{iso}$ = 2.8 and 18.6 ppm have been unambiguously assigned to pseudotetrahedral coordinated interstitial boron (Q*) and tricoordinated interstitial boron (T*), respectively (Scheme 1). By the same token, we can assign the signals at $B_2$

**Scheme 1. Possible Boron Species in B-Doped and (B, Ag)-Codoped $TiO_2$**

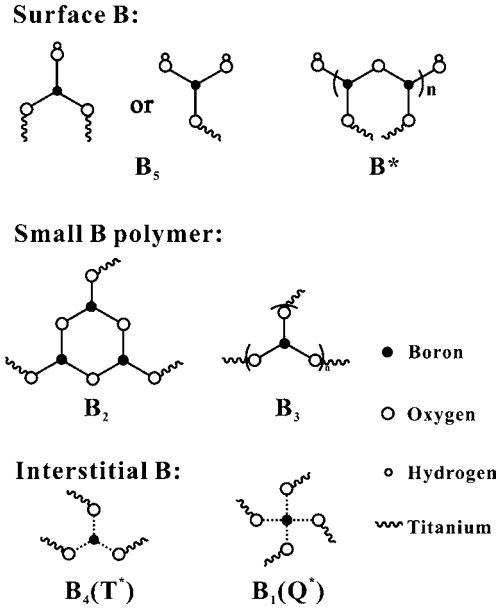


and $B_3$ with $\delta_{iso}$ = 16.8 and 15.9 ppm to borons in the boroxol ring and bulk $BO_{3/2}$ polymer, respectively,[35,36] both of which may exist in the defects or interfaces of the doped $TiO_2$ whereas, the signal at $B_5$ with $\delta_{iso}$ = 20.0 ppm may be attributed to surface B species. Unlike the solely 10% B-doped $TiO_2$, notable variations in the $^{11}B$ 3QZ-FAM MAS NMR spectrum of the (10% B, 3% Ag)-codoped $TiO_2$ (Figure 6b) are observed. In particular, the signal at $B_3$ site disappears. Likewise, the corresponding NMR parameters obtained from spectral deconvolution for the (B, Ag)-codoped $TiO_2$ (Figure 6b, insert) are also summarized in Table 2. It is noteworthy that considerable increases in the asymmetry parameters ($\eta$) of the $B_2$ and $B_4$ (T*) sites are evident upon introducing the secondary dopant (Ag), indicating substantial variations in boron environments.

The spatial proximities of different B sites in various doped $TiO_2$ catalysts were further explored at 18.8 T magnetic field by $^{11}B$ DQ MAS NMR spectroscopy,[19,20,37] as illustrated for the 10% B-doped and the (10% B, 3% Ag)-codoped $TiO_2$ samples shown in Figure 7. The apparent chemical shifts ($\delta_{MAS}$) at 18.8

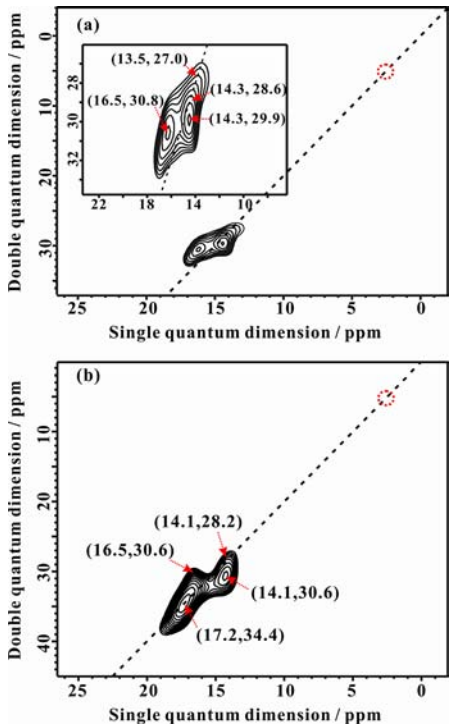


**Figure 7.** $^{11}B$ DQ MAS NMR spectra of (a) 10% B-doped and (b) (10% B, 3% Ag)-codoped $TiO_2$ samples recorded at 18.8 T. The apparent chemical shifts ($\delta_{MAS}$) of various boron species ($B_{1-5}$ and B*) were determined to be 2.4, 14.3, 13.5, 15.6, 16.5, and 17.2 ppm, respectively (see Table 2).

T of various boron species ($B_{1-5}$ sites) in the 10% B-doped $TiO_2$ were determined to be 2.3, 14.3, 13.5, 15.6, and 16.5 ppm, respectively (see Table 2). For the solely B-doped $TiO_2$ (Figure 7a), two diagonal peaks at (13.5, 27.0) and (14.3, 28.6) ppm are observed, corresponding to the autocorrelations of the tricoordinated $B_3$ (bulk $BO_{3/2}$ polymer) and the $B_2$ (boroxol ring) species, respectively. Apart from these autocorrelation peaks, two additional off-diagonal peaks are also observed. The peak located at (14.3, 14.3 + 15.6 = 29.9) ppm corresponds to correlations between $B_2$ and $B_4$ species, indicating a close spatial proximity between the boroxol ring and tricoordinated interstitial (T*) boron species. Another off-diagonal peak at


dx.doi.org/10.1021/ja312205c | J. Am. Chem. Soc. 2013, 135, 1607−1616

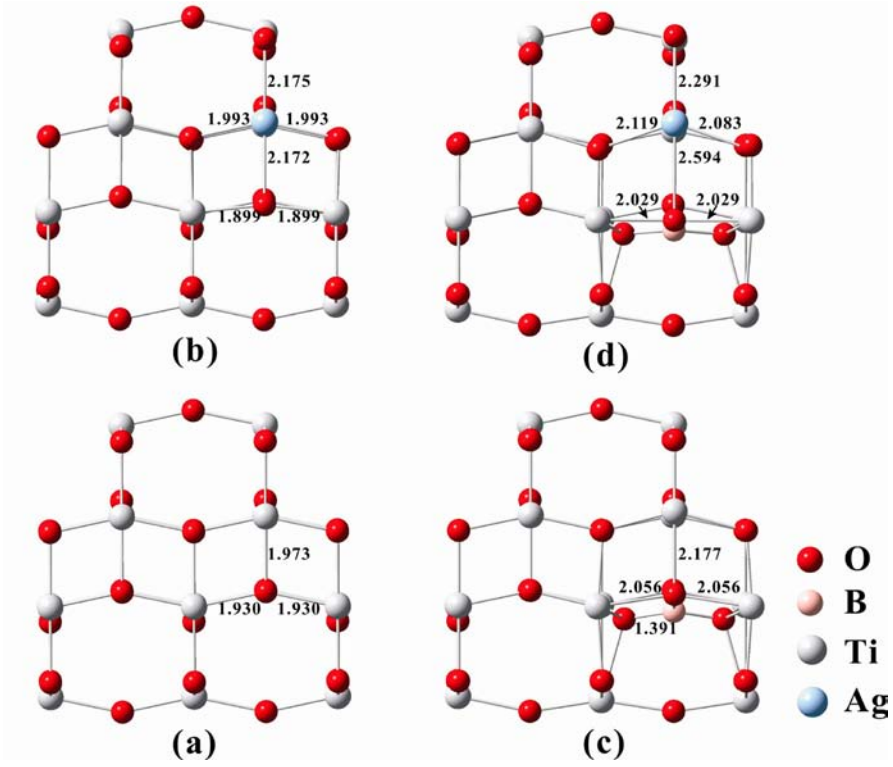


**Figure 8.** Optimized geometries of (a) pure $TiO_2$, and doped-$TiO_2$ incorporated with (b) substitutional Ag, (c) tricoordinated interstitial boron (T*), and (d) the [T*−O−Ag] structural unit.

(16.5, 14.3 + 16.5 = 30.8) ppm indicates that the boroxol ring ($B_2$) species is also in spatial proximity to the surface borons ($B_5$). These results indicate that, for the solely B-doped $TiO_2$, the boroxol ring ($B_2$) species may exist either in the defect sites that are close to the interstitial B (T*) or in the interface sites that are nearby to the surface B species ($B_5$). Interestingly, no autocorrelation peak was observed at (15.6, 31.2) and (2.8, 5.6) ppm, which corresponds to the tri- (T*, $B_4$) and pseudotetrahedral (Q*; $B_1$) coordinated interstitial sites, respectively, indicating the high dispersion of these interstitial B species in the lattice of solely B-doped $TiO_2$.

On the other hand, the $^{11}$B DQ MAS NMR spectrum observed for the (10% B, 3% Ag)-codoped $TiO_2$ catalyst (Figure 7b) is somewhat different from that of solely 10% B-doped $TiO_2$. While the autocorrelation peak representing the $B_2$ species (boroxol ring) at (14.1, 28.2) ppm remains present in the $^{11}$B DQ MAS spectrum, the peak accounting for the $B_3$ species (small $BO_{3/2}$ polymer) is clearly absent. Moreover, an additional autocorrelation peak at (17.2, 34.4) ppm emerges, which is most likely due to the formation of a new surface $BO_{3/2}$ polymer species (i.e., B* site, Scheme 1). The fact that the signal of such a B* site was not observed in the $^{11}$B 3QZ-FAM MAS NMR spectrum (Figure 6b) may be due to its low abundance in the (B, Ag)-codoped catalyst. The absence of the off-diagonal peak at (14.1, 29.4) ppm implies that the boroxol ring ($B_2$) species is no longer in close proximity to the interstitial boron (T*) species ($B_4$) in such (B, Ag)-codoped samples. Nevertheless, the appearance of the off-diagonal peak pairs at (14.1, 30.6) and (16.5, 30.6) ppm reflects that the boroxol ring ($B_2$) species remain in spatial proximity to the surface boron ($B_5$) species. This suggests that the boroxol ring ($B_2$) species that are present originally in the defect sites near the interstitial boron (T*) may disappear upon introducing the secondary Ag, while the boroxol ring ($B_2$) species that are present in the interfaces of the (B, Ag)-doped $TiO_2$ still exist. As such, it is conclusive that upon introducing the secondary Ag dopant into the B-doped $TiO_2$, dramatic variations in local structures of boron took place not only in the interstitial T* ($B_4$) sites but also in the small $BO_{3/2}$ polymers ($B_2$ and $B_3$ sites).

Our XPS results indicate that the Ag dopants are implanted into the crystalline lattice around the interstitial B sites by forming [$B_{int.}$−O−Ag] structural units. Combined with the NMR results, it is further conclusive that the substitutional Ag species should be in close proximity to the tricoordinated interstitial boron (T*) species. When the Ag species substitutes the lattice Ti near the interstitial T* site in the crystalline lattice (leading to formation of [T*−O−Ag] unit), it may also occupy the defects that are originally occupied by the small $BO_{3/2}$ polymers ($B_2$ and $B_3$ sites) in the (B, Ag)-codoped $TiO_2$ due to the large volume of the Ag atom, leading to the absence of $B_2$ and $B_3$ species in the defects. In this context, the majority of the $B_2$ species should exist in the interfaces of the codoped $TiO_2$ that are in close proximity to surface B ($B_5$) species but some distance away from the interstitial boron T* ($B_4$). This is consistent with the absence of cross-correlation peaks between $B_2$ and $B_4$ species, the presence of cross-correlation peaks between $B_2$ and $B_5$ sites in the $^{11}$B DQ MAS NMR spectrum (Figure 7b), and the disappearance of $B_3$ signal in the $^{11}$B 3QZ-FAM MAS NMR spectrum (Figure 6b) of the (10% B, 3% Ag)-codoped $TiO_2$.

**3.5. Calculation of Density of States (DOS).** To verify the role of such [T*−O−Ag] structural units on the extraordinary photocatalytic activity observed for the (B, Ag)-codoped $TiO_2$, theoretical density functional theory (DFT) calculations were employed. Based on their optimized


dx.doi.org/10.1021/ja312205c | J. Am. Chem. Soc. 2013, 135, 1607−1616

structures (Figure 8), the density of states (DOS) of pure $TiO_2$ and doped-$TiO_2$ incorporated with substitutional Ag, tricoordinated interstitial boron (T*), and [T*−O−Ag] were calculated, and the results are shown in Figure 9. As shown

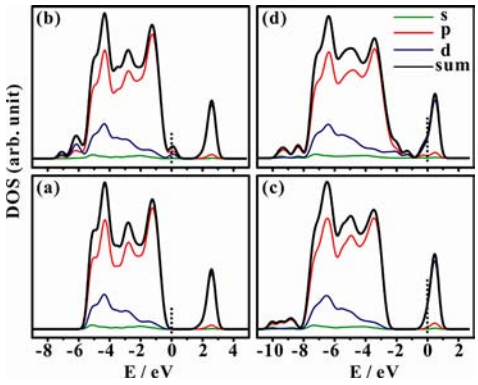


**Figure 9.** Density of states of (a) pure $TiO_2$, and doped-$TiO_2$ associated with (b) substitutional Ag, (c) tricoordinated interstitial boron T*, and (d) T*−O−Ag.

in Figure 9a, for the DOS of pure $TiO_2$, the valence band (VB) and conduction band (CB) mainly consist of O 2p and Ti 3d states.[38] Upon doping Ag ions into the lattice of the $TiO_2$ crystal, an apparent contribution of the Ag 4d states to the formation of impurity energy levels hybridized by the O 2p and Ti 3d states is evident. Compared with the pure $TiO_2$ (Figure 9a), the DOS of substitutional Ag shows new electronic states, which mainly consist of Ag 4d and O 2p states referred to as (Ag 4d, O 2p), above the top of the valence band at 0 eV by mixing states (Figure 9b), which may favor the visible-light absorption and trapping of the photoinduced carriers. Upon doping interstitial boron T* into the $TiO_2$ supercell, no such new electronic states are present in the band gap (Figure 9c), indicating that the interstitial boron T* doping does not favor the visible-light absorption, which is consistent with previous experimental results.[32] It was reported that the visible-light absorption of the solely B-doped $TiO_2$ sample could be ascribed to the presence of interstitial boron Q* and oxygen vacancy.[7,34] It is interesting to note (see Figure 9d) that the presence of the [T*−O−Ag] structural unit can introduce more new electronic states in the gaps between VB and CB due to the contribution of the Ag 4d and B 2s/2p states, corresponding to the formation of impurity energy levels hybridized by the O 2p and Ti 3d states. As a result, the band gap is effectively narrowed. As confirmed by the aforediscussed in situ XPS results, these new states are responsible for trapping the photoinduced carriers and hence prolonging their lifetimes. In other words, such shallow trapping of photoinduced electrons under UV−vis irradiation tends to result in an increase of electron density in the outer layer of the B and Ag atoms in the [T*−O−Ag] structural units. As the outer-layer electron density increases, the shielding effect on the nuclear charge of the light element (B) increases, leading to a decrease of B 1s BE of the inner shell electrons. For the heavy element (Ag), apart from the shielding effect, the increase of the outer-layer electron density also hinders the escape of the inner shell electrons. This may lead to an increase of Ag 3d BE of the inner shell electrons and hence the observed chemical shift of the peaks. In addition, the new states of [T*−O−Ag] in the band gap are largely overlapped with the band states of $TiO_2$, facilitating the transfer of photoinduced carriers within their lifetime.[5] Thus, it can be conclusive that the presence of the [T*−O−Ag] structural unit is responsible for the excellent photocatalytic activity observed for the (B, Ag)-codoped $TiO_2$ compared to the solely B- or Ag-doped $TiO_2$ catalysts.

According to our Ag 3d XPS results, two types of dopant Ag species, substitutional Ag ($Ag^{3+}$) around interstitial B (corresponding to the [$B_{int.}$−O−Ag] structural unit) and metallic Ag ($Ag^0$), are present in the (B, Ag)-codoped $TiO_2$. The metallic Ag would lead to surface plasmonic effects, and the substitutional Ag ($Ag^{3+}$) can introduce new electronic states in the band gap. Both of them can enhance the visible-light absorption of (B, Ag)-codoped $TiO_2$ photocatalysts. Because only metallic Ag species exists in the solely Ag-doped $TiO_2$ samples, as shown in Figure 1, the visible-light absorption obviously increases with increasing the amount of dopant Ag from 1% to 3%, which can be solely ascribed to the increase of the plasmonic effect. As revealed by our XPS experiments, about 0.45% metallic Ag and 2.55% substitutional Ag ($Ag^{3+}$) are present in the (10% B, 3% Ag)-codoped $TiO_2$ sample. In other words, the plasmonic effect from the metallic Ag in this sample should be much lower than that in the 1% Ag-doped $TiO_2$. It is noteworthy that the visible-light absorption of (10% B, 3% Ag)-codoped $TiO_2$ is much higher than that of 1% Ag -doped $TiO_2$ sample (see Figure 1). Therefore, the enhancement of visible-light absorption can be mainly attributed to the presence of the substitutional Ag ($Ag^{3+}$). In addition, limited visible-light activities were observed in the solely Ag-doped $TiO_2$ samples (Figure 2 and Figure S4), indicating that the plasmonic effect of metallic Ag leads to limited visible-light activity. Therefore, we can conclude that the remarkable enhancement of the photoactivity of the (10% B, 3% Ag)-codoped $TiO_2$ sample should be mainly due to the synergistic effect of B and Ag dopants.

**3.6. Electron/Hole Transfer Mechanism.** The above experimental and theoretical results therefore allow us to postulate an electron/hole transfer mechanism for the (B, Ag)-codoped $TiO_2$ photocatalyst under solar-light irradiation, as illustrated in Scheme 2. Upon the irradiation, the [T*−O−Ag]

**Scheme 2. Electron/Hole Transfer Mechanism for the (B, Ag)-Codoped $TiO_2$ Photocatalyst under Irradiation from a Solar-Light Source**

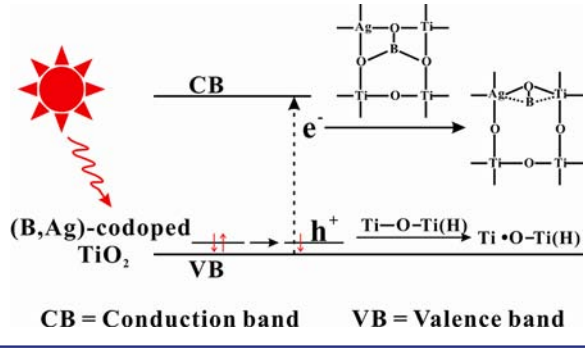


structural unit tends to trap a photoinduced electron to form a intermediate, and the intermediate associated with the new B 1s XPS peak at 190.8 eV (Figure 4b and 4d) may correspond to a Ag−B−O structure (Scheme 2), similar to the structure of interstitial N (Ti−N−O) in N-doped $TiO_2$,[6,39] while its counterpart, namely the photoinduced hole, can diffuse efficiently to the surfaces of the catalyst and react with the


dx.doi.org/10.1021/ja312205c | J. Am. Chem. Soc. 2013, 135, 1607−1616

surface species (such as surface lattice oxygen (Ti−O−Ti) and surface hydroxyls (Ti−O−H)). Indeed, a blueshift (ca. 0.3 eV) of the binding energy of the surface oxygen (529.7 eV) is observable after UV−vis irradiation in the in situ O 1s XPS spectrum (Figure S5b, Supporting Information) of (10% B, 3% Ag)-codoped $TiO_2$, indicating that the surface species do react with the photoinduced hole. Such a blueshift is not observed in the solely Ag-doped $TiO_2$ photocatalyst (Figure S5a, Supporting Information). The presence of [T*−O−Ag] species in the (B, Ag)-codoped $TiO_2$ effectively prolongs the lifetime of the photoinduced carriers and facilitates the efficient transfer of these carriers. Thus, the exceptionally high photocatalytic activity observed for the (B, Ag)-codoped $TiO_2$ catalyst under solar-light irradiation may be unambiguously attributed to the synergistic effect of the B and Ag dopants.

## 4. CONCLUSION

In summary, we found for the first time that boron- and silver-codoped $TiO_2$ photocatalysts exhibit extraordinary reactivity under solar-light irradiation. XPS, $^{11}B$ solid-state NMR spectroscopy, and DFT calculations were employed to gain insight into the origin of the high activity. It was found that parts of dopant B species weave into the interstitial sites of the $TiO_2$ lattice, which favors the incorporation of dopant Ag species into the lattice. As a result, [T*−O−Ag] structural units (T* represents the tricoordinated interstitial boron) were formed in the $TiO_2$ lattice. The presence of the structural units leads to photoinduced shifts of the B 1s, Ag 3d, and Ti 2p peaks upon UV−vis irradiation, due to their trapping of photoinduced electrons. It is anticipated that such a trapping effect can facilitate electron−hole separation and prolong the life of the photoinduced charge carriers, which eventually leads to a considerable enhancement in the catalytic activity. The experimental and theoretical calculation results presented herein should not only facilitate a better understanding of the photocatalytic mechanism at the atomic level but also be helpful for the design of highly active titania-based photocatalysts.

## ■ ASSOCIATED CONTENT

### Supporting Information

The procedure for calculating NMR parameters for various boron species in B-doped and (B, Ag)-codoped $TiO_2$ catalysts; XRD spectra; $H_2$ evolution from methanol solution (5.0 vol %) in the suspension containing pure, B-doped, Ag-doped, and (B, Ag)-codoped $TiO_2$ catalysts; adsorption curves of methylene blue on pure, 10% B-doped, 3% Ag-doped, and (10% B, 3% Ag)-codoped $TiO_2$ in the dark; photodegradation curves of methylene blue on pure and doped $TiO_2$ samples under different types of light irradiation; assorted O 1s in situ XPS spectra of pure and doped $TiO_2$ samples. This material is available free of charge via the Internet at http://pubs.acs.org.

## ■ AUTHOR INFORMATION

### Corresponding Author

dengf@wipm.ac.cn

### Notes

The authors declare no competing financial interest.

## ■ ACKNOWLEDGMENTS

The authors thank National Natural Science Foundation of China (21203240, 21210005, 20933009, 21103223, and 21073228) for financial support and also thank Shanghai Supercomputer Center (SSC, China) and National Center for High-performance Computing (NCHC, Taiwan) for computing facilities.

## ■ REFERENCES

(1) Fujishima, A.; Honda, K. *Nature* **1972**, *238*, 37.
(2) Choi, W.; Termin, A.; Hoffmann, M. R. *J. Phys. Chem.* **1994**, *98*, 13669.
(3) Vamathevan, V.; Amal, R.; Beydoun, D.; Low, G.; McEvoy, S. *J. Photochem. Photobiol., A* **2002**, *148*, 233.
(4) He, C.; Yu, Y.; Hu, X. F.; Larbot, A. *Appl. Surf. Sci.* **2002**, *200*, 239.
(5) Asahi, R.; Morikawa, T.; Ohwaki, T.; Aoki, K.; Taga, Y. *Science* **2001**, *293*, 269.
(6) Livraghi, S.; Paganini, M. C.; Giamello, E.; Selloni, A.; Di Valentin, C.; Pacchioni, G. *J. Am. Chem. Soc.* **2006**, *128*, 15666.
(7) Feng, N.; Zheng, A.; Wang, Q.; Ren, P.; Gao, X.; Liu, S. B.; Shen, Z.; Chen, T.; Deng, F. *J. Phys. Chem. C* **2011**, *115*, 2709.
(8) Rumaiz, A. K.; Woicik, J. C.; Cockayne, E.; Lin, H. Y.; Jaffari, G. H.; Shah, S. I. *Appl. Phys. Lett.* **2009**, *95*, 262111.
(9) Cronemeyer, D. C. *Phys. Rev.* **1959**, *113*, 1222.
(10) Liu, G.; Zhao, Y.; Sun, C.; Li, F.; Lu, G.; Cheng, H. *Angew. Chem., Int. Ed.* **2008**, *47*, 4516.
(11) Reyes-Garcia, E. A.; Sun, Y.; Raftery, D. *J. Phys. Chem. C* **2007**, *111*, 17146.
(12) Ling, Q.; Sun, J.; Zhou, Q.; Ren, H.; Zhao, Q. *Appl. Surf. Sci.* **2008**, *254*, 6731.
(13) Zhao, W.; Ma, W.; Chen, C.; Zhao, J.; Shuai, Z. *J. Am. Chem. Soc.* **2004**, *126*, 4782.
(14) Frydman, L.; Harwood, J. S. *J. Am. Chem. Soc.* **1995**, *117*, 5367.
(15) Medek, A.; Harwood, J. S.; Frydman, L. *J. Am. Chem. Soc.* **1995**, *117*, 12779.
(16) Madhu, P. K.; Goldbourt, A.; Frydman, L.; Vega, S. *Chem. Phys. Lett.* **1999**, *307*, 41.
(17) Madhu, P. K.; Goldbourt, A.; Frydman, L.; Vega, S. *Chem. Phys. Lett.* **2000**, *112*, 2377.
(18) Schnell, I.; Brown, S. P.; Low, H. Y.; Ishida, H.; Spiess, H. W. *J. Am. Chem. Soc.* **1998**, *120*, 11784.
(19) Brown, S. P.; Spiess, H. W. *Chem. Rev.* **2001**, *101*, 4125.
(20) Wang, Q.; Hu, B.; Lafon, O.; Trébosc, J.; Deng, F.; Amoureux, J. P. *J. Magn. Reson.* **2009**, *200*, 251.
(21) Perdew, J. P.; Burke, K.; Ernzerhof, M. *Phys. Rev. Lett.* **1996**, *77*, 3865.
(22) Perdew, J. P.; Ruzsinszky, A.; Csonka, G. I.; Vydrov, O. A.; Scuseria, G. E.; Constantin, L.; Zhou, X.; Burke, K. *Phys. Rev. Lett.* **2008**, *100*, 136406.
(23) Monkhorst, H.; Pack, J. D. *Phys. Rev. B* **1976**, *13*, 5188.
(24) Zhang, L.; Yu, J. C.; Yip, H.; Li, Q.; Kwong, K.; Xu, A.; Wong, P. *Langmuir* **2003**, *19*, 10372.
(25) Wagner, C. D.; Riggs, W. M.; Davis, L. E.; Moulder, J. F.; Muilenberg, G. E. *Handbook of X-ray Photoelectron Spectroscopy*; Perkin-Elmer Corporation: Eden Prairie, MN, 1979; p 112.
(26) Zhang, H.; Wang, G.; Chen, D.; Lv, X.; Li, J. *Chem. Mater.* **2008**, *20*, 6543.
(27) Priya, R.; Baiju, K. V.; Shukla, S.; Biju, S.; Reddy, M. L. P.; Patil, K.; Warrier, K. G. K. *J. Phys. Chem. C* **2009**, *113*, 6243.
(28) Zhang, Q.; Sun, C.; Zhao, Y.; Zhou, S.; Hu, X.; Chen, P. *Environ. Sci. Technol.* **2010**, *44*, 8270.
(29) Taing, J.; Cheng, M. H.; Hemminger, J. C. *ACS Nano* **2011**, *5*, 6325.
(30) Xin, B.; Jing, L.; Ren, Z.; Wang, B.; Fu, H. *J. Phys. Chem. B* **2005**, *109*, 2805.
(31) Burkhard, S.; Martin, J. *Angew. Chem., Int. Ed. Engl.* **1985**, *24*, 118.

(32) Chen, D.; Yang, D.; Wang, Q.; Jiang, Z. *Ind. Eng. Chem. Res.* **2006**, *45*, 4110.
(33) In, S.; Orlov, A.; Berg, R.; Garcia, F.; Pedrosa-Jimenez, S.; Tikhov, M. S.; Wright, D. S.; Lambert, R. M. *J. Am. Chem. Soc.* **2007**, *129*, 13790.
(34) Finazzi, E.; Di Valentin, C.; Pacchioni, G. *J. Phys. Chem. C* **2009**, *113*, 220.
(35) (a) Youngman, R. E.; Zwanziger, J. W. *J. Non-Cryst. Solids* **1994**, *168*, 293. (b) Youngman, R. E.; Haubrich, S. T.; Zwanziger, J. W.; Janicke, M. T.; Chmelka, B. F. *Science* **1995**, *269*, 1416.
(36) Kroeker, S.; Stebbins, J. F. *Inorg. Chem.* **2001**, *40*, 6239.
(37) Yu, Z. W.; Zheng, A. M.; Wang, Q.; Chen, L.; Xu, J.; Amoureux, J. P.; Deng, F. *Angew. Chem., Int. Ed.* **2010**, *49*, 8657.
(38) Asahi, R.; Taga, Y.; Mannstadt, W.; Freeman, A. *Phys. Rev. B* **2000**, *61*, 7459.
(39) Di Valentin, C.; Pacchioni, G.; Selloni, A.; Livraghi, S.; Giamello, E. *J. Phy. Chem. B* **2005**, *109*, 11414.